A&A 577, A62 (2015)
DOI: 10.1051/0004-6361/201525729

Astronomy & Astrophysics

Spectrally resolved detection of sodium in the atmosphere of HD 189733b with the HARPS spectrograph⋆

A. Wyttenbach, D. Ehrenreich, C. Lovis, S. Udry, and F. Pepe

Geneva Observatory, University of Geneva, Ch. des Maillettes 51, 1290 Versoix, Switzerland
e-mail: aurelien.wyttenbach@unige.ch

Received 23 January 2015 / Accepted 14 March 2015

ABSTRACT

Context. Atmospheric properties of exoplanets can be constrained with transit spectroscopy. At low spectral resolution, this technique is limited by the presence of clouds. The signature of atomic sodium (Na I), known to be present above the clouds, is a powerful probe of the upper atmosphere, where it can be best detected and characterized at high spectral resolution.
Aims. Our goal is to obtain a high-resolution transit spectrum of HD 189733b in the region around the resonance doublet of Na I at 589 nm, to characterize the absorption signature that was previously detected from space at low resolution.
Methods. We analyzed archival transit data of HD 189733b obtained with the HARPS spectrograph ($\mathcal{R}$ = 115 000) at the ESO 3.6-m telescope. We performed differential spectroscopy to retrieve the transit spectrum and light curve of the planet, implementing corrections for telluric contamination and planetary orbital motion. We compared our results to synthetic transit spectra calculated from isothermal models of the planetary atmosphere.
Results. We spectrally resolve the Na I D doublet and measure line contrasts of 0.64 ± 0.07% (D2) and 0.40 ± 0.07% (D1) and FWHMs of 0.52 ± 0.08 Å. This corresponds to a detection at the 10σ level of excess of absorption of 0.32 ± 0.03% in a passband of 2 × 0.75 Å centered on each line. We derive temperatures of 2600 ± 600 K and 3270 ± 330 K at altitudes of 9800 ± 2800 and 12 700 ± 2600 km in the Na I D1 and D2 line cores, respectively. We measure a temperature gradient of ~0.2 K km^{-1} in the region where the sodium absorption dominates the haze absorption from a comparison with theoretical models. We also detect a blueshift of 0.16 ± 0.04 Å (4σ) in the line positions. This blueshift may be the result of winds blowing at 8 ± 2 km s^{-1} in the upper layers of the atmosphere.
Conclusions. We demonstrate the relevance of studying exoplanet atmospheres with high-resolution spectrographs mounted on 4-m-class telescopes. Our results pave the way for an in-depth characterization of physical conditions in the atmospheres of many exoplanetary systems with future spectrographs such as ESPRESSO on the VLT or HiReS and METIS on the E-ELT.

Key words. planets and satellites: atmospheres – planets and satellites: individual: HD 189733b – techniques: spectroscopic – instrumentation: spectrographs – methods: observational

1. Introduction

After two decades and over a thousand exoplanet detections, we have entered an era in which these remote worlds can be characterized. More and more exoplanets have precise mass and radius measurements thanks to simultaneous radial-velocity and transit observations, providing estimates of mean densities and constraints on possible bulk compositions. Meanwhile, detections and studies of exoplanet atmospheres represent the only direct observable window we have on the physical and chemical properties of these planets. Characterization of exoplanets and comparative planetology are now progressing well by virtue of advanced instrumentation. Among these observations, spectra of exoplanets are among the best products for an in-depth comprehension of atmospheric and surface conditions.

Shortly after the first indirect exoplanet discoveries, early observational campaigns encouraged by theoretical work (Marley et al. 1999; Seager & Sasselov 2000; Brown 2001) attempted to detect reflected light from the dayside (Charbonneau et al. 1999) or absorption through limb transmission (Moutou et al. 2001). Observations of HD 209458, the only transiting system known at that time, with the Space Telescope Imaging Spectrograph (STIS) onboard the 2.4 m *Hubble* Space Telescope (HST), allowed Charbonneau et al. (2002) to detect atmospheric sodium (Na I) at 589 nm. This measurement was performed with a spectral resolution of $\mathcal{R} \equiv \lambda/\Delta\lambda \sim$ 5500 (or ~55 km s^{-1}). Additional absorption of 0.023 ± 0.006% and 0.013 ± 0.004% has been measured during transits over spectral bins of 12 Å and 38 Å, respectively. The Na I doublet lines D1 (λ589.5924 nm) and D2 (λ588.9951 nm) are not resolved in these bins.

In addition to important detections of other atomic and molecular signatures (e.g., Vidal-Madjar et al. 2003; Deming et al. 2013), the sodium signature in HD 209458b has remained one of the most robust examples of atmospheric characterization (Madhusudhan et al. 2014; Heng & Showman 2014; Pepe et al. 2014). It has been confirmed by independent analysis of the same data set (Sing et al. 2008a,b). In the early days, ground-based observations of transiting systems with high-resolution spectrographs mounted on 8-m-class telescope were also quickly tested with the aim of confirming detections and resolving transmission spectra, unfortunately without any positive results (e.g., Narita et al. 2005). Indeed, even with a high enough signal, no good observational strategy or data analysis were found to overcome terrestrial atmospheric variation and telluric line

⋆ Using observations with the Harps spectrograph from the ESO 3.6 m installed at La Silla, in Chile, under the allocated programmes 072.C-0488(E), 079.C-0828(A) and 079.C-0127(A).

Table 1. Observations log for HD 189733.

	Date	# Spectra[a]	Exp. time [s]	Airmass	Seeing	S/N^b	S/N^c	Program	Analysis
Night 1	2006-09-07	20 (9/11)	900 to 600	1.6–2.1	0.7–1.0	~170	~32	072.C-0488(E)	Yes
Night 2	2007-07-19	39 (18/21)	300	2.4–1.6	0.6–0.8	~110	~20	079.C-0828(A)	Yes
Night 3	2007-08-28	40 (19/21)	300	2.2–1.6	0.7–2.0	~100	~18	079.C-0127(A)	Yes
Night 4	2006-07-29	12 (5/7)	600	1.8–1.6	0.9–1.2	~140	~27	072.C-0488(E)	No

Notes. Three transit events are analyzed in our work. [(a)] In parenthesis: the number of spectra taken during the transit (forming our in-transit sample) and outside the transit (forming our out-of-transit sample). [(b)] The signal-to-noise ratio (S/N) per extracted pixel in the continuum near 590 nm. [(c)] The S/N in the line cores of the Na I D doublet (this shows the first difficulty of sodium detection in exoplanet atmospheres).

contamination that transmission spectra undergo. Later, careful data (re-)analysis made by Redfield et al. (2008) and Snellen et al. (2008) enabled overcoming the systematics that are due to the terrestrial atmosphere and led to the first ground-based detection of an exoplanet atmospheric signature. The Na I doublet was detected for the first time in HD 189733b with the High Resolution Spectrograph (HRS; $\mathcal{R} \sim 60\,000$) mounted on the 9 m Hobby-Eberly Telescope and was confirmed in HD 209458b using the High Dispersion Spectrograph (HDS; $\mathcal{R} \sim 45\,000$) on the 8 m Subaru telescope. Furthermore, the analysis of the space-based detection of the sodium signature of these two planets by Sing et al. (2008b), Vidal-Madjar et al. (2011), and Huitson et al. (2012), demonstrated the potential of resolving the transmitted stellar light by the planet atmosphere. Despite these encouraging works, the presence of scattering hazes and clouds (Lecavelier Des Etangs et al. 2008a,b; Pont et al. 2013) in several exoplanets prevented the detection of major chemical constituents at low to medium resolution even from space (e.g., Kreidberg et al. 2014; Sing et al. 2015). The whole potential of high-resolution spectroscopy with $R \sim 100\,000$ applied to transiting and nontransiting system was shown when H_2O and CO molecular bands were detected by cross-correlating hundreds of resolved individual transitions (Snellen et al. 2010, 2014; Brogi et al. 2012; Birkby et al. 2013). This advanced method refocused the attention on the importance of transit spectroscopy observations from the ground.

Transit spectroscopy with ground-based telescopes is often used to gauge the Rossiter-McLaughlin effect during an exoplanet transit. This is accomplished with high-precision velocimeters. As data are acquired during transit, we can think about measuring exoplanet atmosphere properties with the same data. However, observations with simultaneously calibrated or self-calibrated velocimeter are not equally valuable because of the use of an iodine cell. The absorption of light by the iodine cell acts as a contaminant. The iodine lines prevent measuring several spectral features, especially around the Na I lines. Thus the use of stabilized spectrographs with simultaneous calibration enables measuring the Rossiter-McLaughlin effect and the transmission spectrum of an exoplanet at the same time.

We here describe new results obtained with the HARPS spectrograph from analyzing existing high-quality Rossiter-McLaughlin observations of HD 189733b. For the first time, features in an exoplanet atmosphere are resolved with a 4 m-class telescope. In Sect. 2, we present the observations, the data reduction, the telluric correction, and the method for measuring exo-atmospheric signals. In Sect. 3, we describe the results obtained from the measure of the Na I D absorption excess in HD 189733b. In Sect. 4, we discuss the implication of our detection, and finally, we compare our results with theory.

2. Observations, data reduction and methods

2.1. HARPS observations

HD 189733 (Bouchy et al. 2005) was observed with the High-Accuracy Radial-velocity Planet Searcher (HARPS) echelle spectrograph on the ESO 3.6 m telescope, La Silla, in Chile (Mayor et al. 2003). Data were retrieved from the ESO archive from programs 072.C-0488(E), 079.C-0127(A) (PI:Mayor), and 079.C-0828(A) (PI: Lecavelier des Etangs). The data sets are described in Table 1 (nights 1, 3, and 4 were employed by Triaud et al. 2009 to measure the Rossiter-McLaughlin effect). In total, four sequences of data cover the transit of the planet at least partially. Of these four sequences, two were obtained using low-cadence (600 s) exposures, the two others using high-cadence (300 s) exposures. One low-cadence sequence was affected by bad weather and missed the second half of the transit. For this reason, we decided not to take this sequence (2006-07-29) into account. Our analysis is based on the remaining three data sequences that cover 99 spectra and 3 planetary transits in total. Based on the transit ephemeris of Agol et al. (2010; see Table 2), we identified 46 spectra fully obtained in transit (i.e., fully between the first and fourth contacts). The 53 remaining spectra constitute our out-of-transit sample.

2.2. Data reduction

The HARPS observations were reduced with version 3.5 of the HARPS data reduction software. Spectra were extracted order by order and flat fielded with the daily calibration set. Each spectral order was blaze corrected and wavelength calibrated. All spectral orders from a given two-dimensional echelle spectrum were merged and resampled with a 0.01 Å wavelength step into a one-dimensional spectrum. Flux is conserved during this step. A reduced HARPS spectrum covers the region between 380 nm and 690 nm with a spectral resolution of $\mathcal{R} \sim 115\,000$ or 2.7 km s^{-1}. All spectra refer to the solar system barycenter rest frame, and wavelengths are given in the air.

As we show in Sect. 2.4, the next step was to separately co-add the in-transit spectra on the one hand and the out-of-transit spectra on the other hand to build the master-in and master-out spectra. The ratio of the master-in and the master-out spectra yields the transmission spectrum. Then, any changes in the stellar line shape or position during the observations can create spurious signals in the transmission spectra, which can become false-positives of atmospheric signals (i.e., with similar amplitude). This is the case for changes in the line spread function (LSF) of the instrument. Here the spectrograph design is important: HARPS is a fiber-fed spectrograph stabilized in temperature and pressure, ensuring that changes in the point

Table 2. Adopted values for the orbital and physical parameters of HD 189733b.

Parameters	Symbol	Values	Units	References
Transit epoch (BJD)	T_0	2 454 279.436714 ± 0.000015	days	Agol et al. (2010)
Orbital period	P	2.21857567 ± 0.00000015	days	Agol et al. (2010)
Planet/star area ratio	$(R_p/R_s)^2$	0.02391 ± 0.00007		Torres et al. (2008)
Transit duration	t_T	0.07527 ± 0.00037	days	Triaud et al. (2009)
Impact parameter	b	0.6631 ± 0.0023	$R_\star$	Agol et al. (2010)
Orbital semi-major axis	a	0.0312 ± 0.00037	AU	Triaud et al. (2009)
Orbital inclination	i	85.710 ± 0.024	degrees	Agol et al. (2010)
Orbital eccentricity	e	0		fixed
Longitude of periastron	ω	90	degrees	fixed
Stellar velocity semi-amplitude	K_1	200.56 ± 0.88	km s^{-1}	Boisse et al. (2009)
Systemic velocity	γ	−2.2765 ± 0.0017	km s^{-1}	Boisse et al. (2009)
Stellar mass	$M_\star$	0.823 ± 0.029	$M_\odot$	Triaud et al. (2009)
Stellar radius	$R_\star$	0.756 ± 0.018	$R_\odot$	Torres et al. (2008)
Planet mass	M_P	1.138 ± 0.025	M_J	Triaud et al. (2009)
Planet radius	R_P	1.138 ± 0.027	R_J	Torres et al. (2008)

spread function (PSF) between two consecutive observations lead to negligible changes in the LSF at timescales of one night. Nonetheless, change in the line positions are due to the radial-velocity variation of the star during the transit of the planet (~50 m s^{-1}). This must be removed before computing the transmission spectra. Omitting this step for spectral shifts of 0.01 Å or larger creates artificial signals. We corrected from this effect by shifting the spectra to the null stellar radial velocity (i.e., the mid-transit stellar radial velocity) according to a Keplerian model of the targeted planetary system (see the model parameters in Table 2). Another source of change in the stellar line shape is the Rossiter-McLaughlin effect. As the transit occurs, the planet occults different parts of the stellar disk that have different intrinsic line shapes and shifts. False-positive features will then appear in the transmission spectrum even if the stellar spectra are well aligned. A way to overcome this difficulty is to register spectra uniformly during the transit, so that this effect will be averaged out during a full transit.

2.3. Telluric correction

High-resolution spectra recorded from the ground bear the imprint of Earth's atmosphere. In the visible domain covered with HARPS, water vapor and molecular oxygen are the main contributors to this time-variable telluric contamination. Variation in the transmission of Earth's atmosphere during a night depends on the airmass and on water column variations in the air. In addition to the contaminating water lines around the Na I doublet, we expect the observed spectra to also possess a signature of the telluric sodium (Vidal-Madjar et al. 2010). Even if the telluric sodium undergoes seasonal variations and possibly does not follow the water absorption levels, we assume that within a night, this telluric sodium absorption behaves and can be corrected for as other telluric features (Snellen et al. 2008; Zhou & Bayliss 2012). Furthermore, visual inspection of our telluric spectra did not reveal any obvious telluric sodium features.

Telluric contamination produces ubiquitous features in transmission spectra. However, the telluric features can be removed by subtracting high-quality telluric spectra obtained on the same nights. As our observed spectra refer to the solar system barycentric rest frame, the telluric lines were shifted during the three different nights by –0.26 Å, 0.09 Å, and –0.19 Å compared to their rest frame. Methods described in Vidal-Madjar et al. (2010) and Astudillo-Defru & Rojo (2013) enabled us to build high-quality telluric spectra night by night using the HARPS observations themselves. Both methods consider that the variation of telluric lines linearly follows the airmass variation. This is a consequence of the usual hypothesis of a radiative transfer in a plane-parallel atmosphere. It implies that apart from different constructions of telluric spectrum, these methods yield equivalent telluric spectra. Similarly, we built for each night a reference telluric spectrum $T(\lambda)$ such as

$$T(\lambda) = T^1(\lambda) \equiv \mathrm{e}^{Nk_\lambda}, \quad (1)$$

corresponding to a zenithal atmospheric transmission (airmass $\sec z = 1$). The zenithal optical depth Nk_λ was derived at each wavelength λ by linear regression on the logarithm of the normalized flux $\log F(\lambda)$ as a function of $\sec z$ (Astudillo-Defru & Rojo 2013). The computed telluric spectra (see Fig. 1) are consistent with the atmospheric transmission obtained by Hinkle et al. (2003). Note that the telluric spectra are built with the out-of-transit sample alone. This is important to avoid overcorrecting for the possible exoplanet atmosphere we search for. However, for night 2, we had to take the in-transit sample into account because the base line was insufficient for computing a high-quality telluric spectrum (during this night, there was no observation before transit).

Taking advantage of the scaling relation between the telluric line strength and the airmass, we corrected the spectra for telluric contamination. Corrections were made by rescaling all spectra as if they had been observed at the same airmass. To obtain this spectrum F_{ref} at airmass $\sec z_{\mathrm{ref}}$, we divided the observed spectra $O_{\sec z}(\lambda)$ taken at airmass $\sec z$ by the telluric reference spectrum to the power $\sec z - \sec z_{\mathrm{ref}}$:

$$F_{\mathrm{ref}}(\lambda) = O_{\sec z}(\lambda)/T(\lambda)^{\sec z - \sec z_{\mathrm{ref}}}. \quad (2)$$

We fixed the reference airmass to the average airmass of the in-transit spectra. This ensures both a telluric correction and minimal flux changes in the reduced spectra. If the quality and stability of the observation nights are good enough, which typically depends on a constant water atmospheric content, this method is sufficient to correct down to the statistical noise level. However, the quality of the nights are generally not sufficient because second-order variations of telluric lines are present and telluric

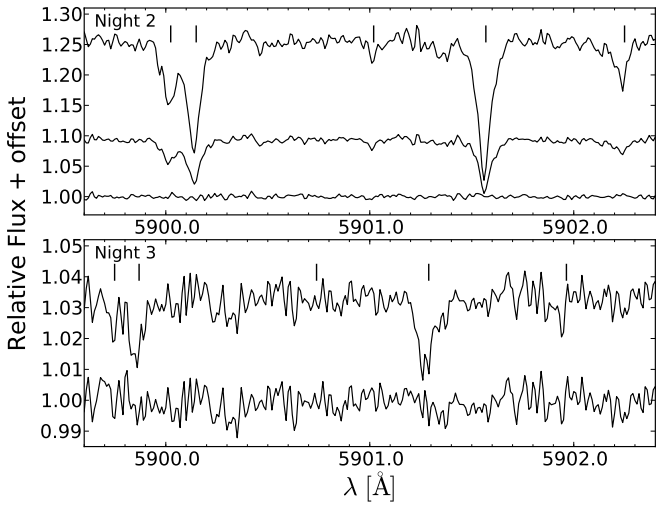

Fig. 1. Example of the effect of the terrestrial atmosphere on exoplanetary transmission spectra. This shows the importance of a precise telluric correction. *Upper panel*: calculated telluric spectrum $T(\lambda)$ (top), transmission spectrum without any correction (middle), and transmission spectrum with the telluric correction (bottom) for night 2. The telluric lines dominate all features in the uncorrected transmission spectrum. *Lower panel*: transmission spectra with telluric corrections already performed for night 3. After we apply the telluric correction described in Sect. 2.3 (airmass effect) we obtain a transmission spectra with weak telluric line residuals (top). Since residuals of telluric lines are still visible, we apply a second telluric correction (correction for features due to water column variation, see Sect. 2.4). This enables us to obtain a transmission spectrum corrected for the effect of the terrestrial atmosphere (bottom). Note the different vertical scales. Some evident telluric lines are emphasized with vertical lines. The telluric lines are shifted from one night to the other because the spectra refer to the solar system barycenter rest frame and were not observed at the same barycentric terrestrial radial velocity.

residual can still be visible in transmission spectra (see Fig. 1 and Sect. 2.4). These observation were not planned to observe exoplanetary atmospheres, but Rossiter-McLaughlin effects. This is less demanding in terms of sky quality and requires a shorter time baseline. Later in our analysis, we performed a second telluric correction to remove possible telluric residuals.

2.4. Transmission spectrum

Transit spectroscopy is a differential technique requiring the acquisition of spectra during and outside transit events. Ground-based observations out-of-transit ($O_{\rm out}$) contain the stellar light absorbed by the terrestrial atmosphere. Observations during transit ($O_{\rm in}$) additionally contain the exoplanet atmosphere transmission diluted into the stellar flux. Stacking telluric-corrected spectra in-transit ($F_{\rm in}$) and out-of-transit ($F_{\rm out}$) allows obtaining master-in ($\mathcal{F}_{\rm in}$) and master-out spectra ($\mathcal{F}_{\rm out}$). Classical methods obtain transmission spectra ($\Re' = \Re - 1 = \mathcal{F}_{\rm in}/\mathcal{F}_{\rm out} - 1$) of the exoplanet atmosphere by dividing night by night the master spectrum in-transit by the master spectrum out-of-transit (Redfield et al. 2008). We can then analyze exoplanet atmosphere features along wavelengths of interest. These methods do not consider changes in radial velocity of the planet.

Here, we present a modified approach with respect to Redfield et al. (2008) to correct for this effect. As the planet transits its star, its radial velocity typically changes from -15 km s^{-1} to $+15$ km s^{-1}. Therefore, the planetary atmospheric absorption lines of sodium move from the blueshifted to the redshifted part of the stellar lines. Near the sodium doublet this shift is $\lesssim$0.5 Å during the full transit in the optical. We corrected for this effect in our analysis by shifting the planetary signal to the null radial velocity in the planet rest frame (i.e., the radial velocity of the planet in the mid-transit). Instead of taking the ratio of master spectra, we divided each spectrum in-transit by the master-out, then shifted the residual with the computed planetary radial velocity and summed all the individual transmission spectra. We normalized this sum to unity by a linear fit to the continuum outside the regions of interests. This allowed us to compute the transmission spectra as

$$\Re'(\lambda) = \frac{\mathcal{F}_{\rm in}}{\mathcal{F}_{\rm out}} - 1 = \sum_{\rm in} \frac{F_{\rm in}(\lambda)}{\sum_{\rm out} F_{\rm out}(\lambda)}\Big|_{\rm planet\ RV\ shift} - 1. \quad (3)$$

With this correction, we expect to see the exoplanetary signal at wavelengths corresponding to the systemic velocity rest frame (and not in the solar system rest frame).

A transmission spectrum (with or without radial-velocity correction) corrected for the airmass effect (Sect. 2.3) can still present some telluric line residuals. This is due to water column variations in the air above the telescope. Therefore we applied a second telluric correction to correct for telluric features in the transmission spectra. Because both the transmission spectra and the telluric spectra contain telluric features at corresponding wavelengths, these two spectra are correlated. To eliminate these correlations and the residuals of telluric lines in the transmission spectrum, a linear fit was made between all corresponding fluxes in wavelength of the transmission spectrum and the telluric reference spectrum. The transmission spectrum was then divided by the fit solution. Because only telluric residuals are correlated with the telluric spectrum, doing this iteratively eliminates telluric residuals in the transmission spectra without affecting the other part of the spectra (Snellen et al. 2008, 2010; Khalafinejad 2013). Practically, one iteration is sufficient to reduce atmospheric pollution to the photon-noise level.

2.5. Binned atmospheric absorption depth

To compare our results with previous detections of sodium in HD 189733b (Redfield et al. 2008; Jensen et al. 2011; Huitson et al. 2012) or in other exoplanets (Charbonneau et al. 2002; Snellen et al. 2008; Sing et al. 2008a, 2012, 2015; Langland-Shula et al. 2009; Wood et al. 2011; Zhou & Bayliss 2012; Murgas et al. 2014; Nikolov et al. 2014; Burton et al. 2015), we calculated the relative absorption depth across various bins in wavelength. Taking into account the systemic velocity, we averaged the flux around the central passbands (C) centered on the two lines of the sodium doublet. Here and later in our analysis, all the averages are weighted by the estimated errors on the reduced spectra, which are taken to be random photon noise obeying Poisson statistics. We compared the integrated flux in the transmission spectrum $\Re'(C)$ to bins of similar bandwidths taken in the transmission spectrum continuum. Snellen et al. (2008) chose adjacent control passbands on the blue (B) and red (R) side of the central passband. At high-resolution, exoplanet atmospheric lines are likely to be resolved, therefore we preferred to choose absolute reference passbands outside the sodium doublet, but still on the two sides (B and R) of the transition (see, e.g., Charbonneau et al. 2002). Relative depths due to exo-atmospheric absorption are then obtained from

the difference of fluxes between the central and the reference passband,

$$\delta(\Delta\lambda) = \overline{\Re'(C)} - \frac{\overline{\Re'(B)} + \overline{\Re'(R)}}{2}. \quad (4)$$

Because small passbands encompass only one line, we averaged the absorption depth of the two Na I D lines. When the central passband includes the two lines, we adjusted it to the center of the doublet.

2.6. Transmission light curve

This method consists of directly deriving the relative transmission light curve as a function of time (Charbonneau et al. 2002; Snellen et al. 2008). Thus, the absorption excess due to the exoplanet atmospheric limb can be seen as a relative flux decrease during the transit. This differs from the method presented in Sect. 2.4. The spectrophotometry is performed on individual spectra for a given spectral bin. We obtain time-dependent information, but the wavelength dependence is lost.

For each telluric-corrected stellar spectrum (F), we derived the relative flux at the Na I D lines by comparing fluxes inside passbands in the center, red, and blue part of each lines (see Sects. 2.5 and 3.1 for the description of the passbands):

$$\mathcal{F}_{\rm rel}(t, \Delta\lambda) = \frac{2 \times \overline{F(C)}}{\overline{F(B)} + \overline{F(R)}}. \quad (5)$$

We then normalized the relative timeseries to unity. For the smaller passbands, we averaged the relative fluxes of the two Na I D lines spectrum by spectrum.

Because we always compared the same parts of each spectrum, the relative flux should be constant with time except if absorption by the planetary atmosphere is present during the transit. With this method, we cannot apply any planetary radial-velocity correction. Taking into account the radial-velocity effect would change the central passband, thus it would change the relative flux (not because there is absorption, but because we do not have a constant central passband). However, this only is a potential problem for the smallest passbands for which we can expect a loss of absorption.

Another type of telluric correction was applied to the relative flux sequence. As the telluric absorption changes with airmass, we expect to see correlations between relative fluxes and the airmass, especially when the passbands contain telluric lines. The first correction applied on individual stellar spectra (Sect. 2.3) should have already mitigated this effect. However, some light curves still show correlations with airmass. To remove any residual airmass effect, we modeled the flux variation as a linear function of the airmass and removed the linear trend. If possible, we only considered out-of-transit data to perform our fit.

Astudillo-Defru & Rojo (2013) discussed whether or not fitting a transit model to the data can change the measurement of the absorption depth. They showed that the absorption depth is well measured by simple average differences. Differential stellar limb-darkening does not significantly affect the measurement in such narrow passbands. The transmitted flux or relative depth is then given by the difference of the average of the relative flux in and out of transit:

$$\delta(\Delta\lambda) = \frac{\overline{\mathcal{F}_{\rm rel}(t_{\rm in})}}{\overline{\mathcal{F}_{\rm rel}(t_{\rm out})}} - 1. \quad (6)$$

Integrating the transit light curve over the in-transit duration makes enables comparing the result with the binned atmospheric absorption depths described in Sect. 2.5. Both approaches give similar results because of the normalization processes and the use of photon-noise-weighted averages in the two methods.

2.7. Systematic effects

To measure the uncertainty on the relative absorption depth $\delta(\Delta\lambda)$, we propagated the errors of the reduced spectra through our analysis. We estimated the errors on the reduced spectra as random photon noise obeying Poisson statistics. Systematic effects, on the other hand, probably contribute to the total noise budget. We used different statistical methods, such as an empirical Monte Carlo method (Redfield et al. 2008) or bootstrapping, to estimate the impact of correlated noise. The basic principle of these methods is to randomize data, to artificially create new set of observations, and to feed them to our data analysis.

First, we followed the empirical Monte Carlo technic presented in Redfield et al. (2008). The idea is to see whether or not the measurement is an artifact of the data or if it is really created by the transit and hence due to the planetary companion. We selected a subsample of spectra of all the spectra available in a night. The choice of this sub sample was then fixed (we call it a scenario). Next, this new sample was randomly divided into two parts to create an in-transit and an out-of-transit simulated data set. These two data sets always contain the same number of spectra.

As in Redfield et al. (2008), we explored three scenarios per night. In the first scenario (out-out), the spectra were only selected among the nominal out-of-transit spectra. The number of spectra in the simulated in-transit data compared to the number of spectra in the simulated out-of-transit data have the same proportion as in the nominal observations. As we randomly chose only among the out-of-transit spectra, we expect to find the distribution of computed relative absorption depth centered at zero. Similarly, an in-in scenario was created, but the random in-transit and out-of-transit data were chosen only in the spectrum observed during the transit. As the planetary signal should be present inside every in-transit observation, the final in-in distribution is also expected to be centered at zero. Finally, an in-out scenario was obtained. All the out-of-transit observation form a fixed master-out (the same as the nominal master-out). We randomly chose a subsample of in-transit spectra. Here, we did not fix the number of spectra of the in-transit subsample. This later one is composed of half to the totality of the number of nominal in-transit spectra.

How can the computed distribution be interpreted? Redfield et al. (2008) considered the standard deviation of the out-out distribution as the global error on the transmitted signal. Astudillo-Defru & Rojo (2013) instead considered the standard deviation of the in-out distribution as the error on the transmitted signal. Here, we followed Redfield et al. (2008) and took the out-out scenario to infer the error on our measured absorption depth, because it is independent of any planetary signal. Nevertheless, the errors are overestimated with the standard deviation of the out-out scenario, because in each iteration only a fraction of the data is used. Thus, to derive correct errors on our absorption depth, we divided the standard deviation of the out-out scenario by the square root of the ratio of the total number of spectra to the number of spectra out of transit.

Second, we calculated false-alarm probabilities. We randomized spectra and recreated transmission spectra and light curves (i.e., by randomizing the time sequence) and quantified how many randomized data sets yield a signal as significant as the real

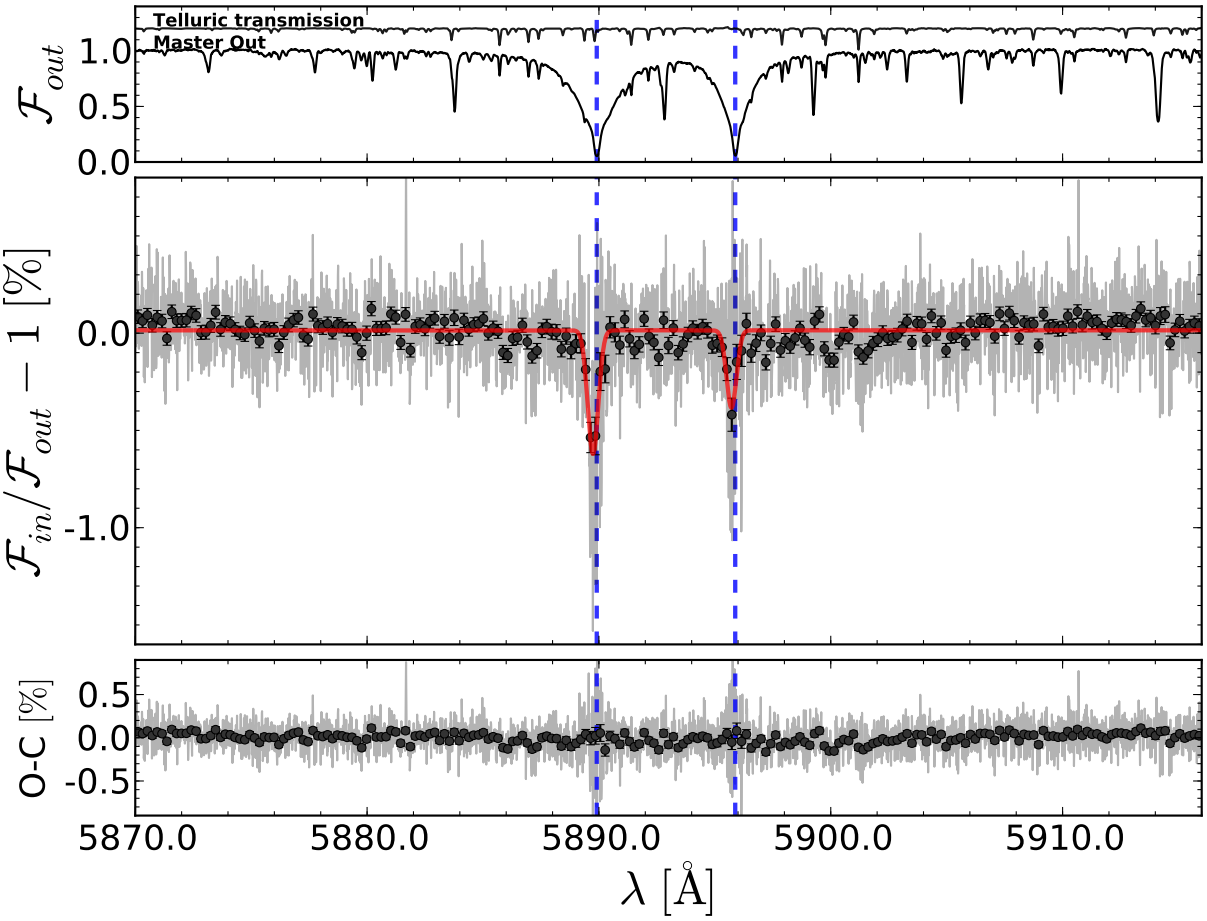

Fig. 2. HARPS transmission spectrum of HD 189733b around the sodium Na I D doublet. *Upper panel*: master-out spectrum (stack of the out-of-transit spectra) normalized to unity. A telluric spectrum is also shown with a vertical offset to be able to identify water telluric lines. *Middle panel*: overall transmission spectrum of the exoplanet atmosphere taking into account all the observing nights (light gray). The transmission spectrum is shown binned by 20× with black circles. The planetary radial-velocity correction is applied. We can easily see the core absorption of the two Na I D lines from the planetary atmosphere. We show a Gaussian fit to each Na I D lines (red). We measure line contrasts of 0.64 ± 0.07% (D2) and 0.40 ± 0.07% (D1) and FWHMs of 0.52 ± 0.08 Å. The transition wavelengths of the doublet in the planet rest frame are indicated with the blue dashed line. A net blueshift is measured from our fit with a value of 0.16 ± 0.04 Å. This blueshift may be due to wind in the upper layer of the atmosphere with a velocity of 8 ± 2 km s^{-1} (see text). *Lower panel*: residuals to the Gaussian fit. The noisy part is centered on the wavelength of the two sodium lines where the stellar flux is the lowest.

measurement. This was done night by night and by considering all the original spectra.

3. Results and analysis

3.1. Na I D detection

We focused on the two transitions of the sodium doublet (D2 at λ5889.951 and D1 at λ5895.924 Å), therefore we restricted the wavelength range for our analysis to the domain from 5870 to 5916 Å. Taking into account the systemic velocity of –2.2765 km s^{-1}, these lines are, in the solar system barycentric rest frame, at λ5889.906 and λ5895.879 Å.

To compute absorption depths, we defined different central passbands (C) composed of two sub-bands centered on each sodium transition line. A total band width of 6 = 2 × 3 Å, 3 = 2 × 1.5 Å, 1.5 = 2 × 0.75 Å, 0.75 = 2 × 0.375 Å and 0.375 = 2 × 0.188 Å were chosen (the 6 = 2 × 3 Å is actually 2 × 2.98 Å). We added to these bands a larger passband of 12 Å to compare our results to those of Redfield et al. (2008), Jensen et al. (2011), and Huitson et al. (2012). Because the 12 Å band encompasses the two sodium lines, we adjusted it on the center of the doublet. For every band, we chose a unique reference passband corresponding to the blue (B) and red (R) adjacent passbands of the central passband of 12 Å (i.e., B = 5874.89–5886.89 Å, R = 5898.89–5910.89 Å).

3.2. Transmission spectrum analysis

The total signal-to-noise ratio (S/N) per extracted pixel of the in and out master spectra ($\mathcal{F}_{\rm in}$ and $\mathcal{F}_{\rm out}$) ranges from 400 to 550 for all nights in the continuum around 589 nm. A pixel on the HARPS detector represents ~0.8 km s^{-1} (or 0.016 Å at 589 nm). The total S/N for each master is about 850 when the nights are co-added. Thus, a final S/N on the transmission spectra ($\Re'$) of about 1200 per extracted pixel is reached. For the transmission spectra, the S/N in the core of the sodium lines decreases to ~260. It is therefore important to co-add the fluxes over tens to hundreds pixels to reach a sufficient S/N for atmospheric detections. We computed different transmission spectra with and without planetary radial-velocity correction. The standard deviation of the transmission spectra was about 2200 ppm for each night in the continuum. When adding the nights, the standard deviation decreases to 1450 ppm. As we can see in Fig. 2, the two exoplanetary sodium lines stand out from the continuum.

Table 3. Summary of the measured relative absorption depth in [%] of the transmission spectra with radial-velocity correction.

$\Delta\lambda$ [Å]	$0.375 = 2 \times 0.188$	$0.75 = 2 \times 0.375$	$1.5 = 2 \times 0.75$	$3 = 2 \times 1.5$	$6 = 2 \times 3$	12
# pixel	$\sim 2 \times 12$	$\sim 2 \times 25$	$\sim 2 \times 50$	$\sim 2 \times 98$	$\sim 2 \times 194$	$\sim$780
Night 1	0.764 ± 0.095	0.532 ± 0.064	0.378 ± 0.046	0.202 ± 0.025	0.115 ± 0.014	0.077 ± 0.010
Night 2	0.495 ± 0.112	0.431 ± 0.077	0.198 ± 0.054	0.028 ± 0.029	0.015 ± 0.017	0.018 ± 0.011
Night 3	0.560 ± 0.104	0.500 ± 0.071	0.415 ± 0.050	0.221 ± 0.027	0.113 ± 0.015	0.080 ± 0.010
All nights	0.571 ± 0.065	0.472 ± 0.044	0.320 ± 0.031	0.141 ± 0.017	0.075 ± 0.010	0.056 ± 0.007

Table 4. Summary of the measured relative absorption depth in [%] of the light curve.

$\Delta\lambda$ [Å]	$0.375 = 2 \times 0.188$	$0.75 = 2 \times 0.375$	$1.5 = 2 \times 0.75$	$3 = 2 \times 1.5$	$6 = 2 \times 3$	12
# pixel	$\sim 2 \times 12$	$\sim 2 \times 25$	$\sim 2 \times 50$	$\sim 2 \times 98$	$\sim 2 \times 194$	$\sim$780
Night 1	0.606 ± 0.179	0.468 ± 0.095	0.339 ± 0.053	0.207 ± 0.031	0.127 ± 0.018	0.064 ± 0.013
Night 2	0.244 ± 0.199	0.165 ± 0.106	0.143 ± 0.059	0.040 ± 0.034	0.027 ± 0.021	0.026 ± 0.014
Night 3	0.521 ± 0.224	0.661 ± 0.119	0.457 ± 0.066	0.274 ± 0.039	0.133 ± 0.023	0.091 ± 0.016
All nights	0.478 ± 0.113	0.451 ± 0.060	0.325 ± 0.033	0.184 ± 0.019	0.102 ± 0.012	0.062 ± 0.008

Without planetary radial-velocity correction, the atmospheric absorption is best detected in our $1.5 = 2 \times 0.75$ Å passband at a level of $0.309 \pm 0.034\%$ (9σ). Our detection in the 12 Å passband is measured at a level of $0.060 \pm 0.008\%$ (7.5σ). Here and in the following, we define absorption as a negative relative depth. With planetary radial-velocity correction, the signal in these same, $1.5 = 2 \times 0.75$, and the 12 Å passbands are $0.320 \pm 0.031\%$ (10.3σ) and $0.056 \pm 0.007\%$ (8σ) (see Table 3). As the radial-velocity correction consists of a wavelength shift smaller than 0.25 Å, it is normal that the integrated signals on these passbands are consistent. Furthermore, our measurements agree with the detection by Huitson et al. (2012) from space ($0.051 \pm 0.006\%$ for the 12 Å passbands) and by Redfield et al. (2008) and Jensen et al. (2011) from ground (0.067 ± 0.020 and 0.053 ± 0.017 for the 12 Å passband).

These absorption signals can be interpreted as equivalent relative altitudes. Altitudes can be inferred by considering the transmission at the limb. The atmospheric absorption (which depends on wavelength) is due to an optically thick layer (presence of an absorber) at a certain height above the measured planetary radius (in the broadband light curve). The height of this layer is generally a few times greater than the atmospheric scale height of the planet ($H = kT/\mu g$) because of the variation with wavelength of the cross-section of the absorber (Lecavelier Des Etangs et al. 2008a). The absorption depths measured in the $1.5 = 2 \times 0.75$ Å passband correspond to an equivalent altitude of 5100 ± 500 km assuming unresolved features. This is about 27 atmospheric scale heights of HD 189733b ($H = 190$ km for 1140 K, the equilibrium temperature of HD 189733b, assuming a mean molecular weight of $\mu = 2.3$ and an albedo of 0.2).

To understand the impact of our radial-velocity correction, we therfore consider the smallest passband. At first glance, integrations over the $0.75 = 2 \times 0.375$ Å and $0.375 = 2 \times 0.188$ Å passbands give us weaker signals than the signals we acquire without radial-velocity correction. This is not expected, since the radial-velocity correction should sum all the absorptions signals and thus strengthen the signal. A closer examination of the transmission spectrum with a Gaussian fitting to each line shows that the exoplanetary sodium lines are blueshifted by about 0.16 Å in the planet rest frame. Integrating the lines including this shift (with the smallest passbands blueshifted) enables recovering the full signal.

What can produce the blueshift of the exoplanetary sodium lines we measure, and is it significant? A global error on the planetary radial-velocity shift is probably lower than 3 km s^{-1} (0.06 Å) considering the HARPS precision on the stellar radial-velocity propagated to the planet. Our 0.16 Å value is much lower than the ~0.75 Å measured by Redfield et al. (2008). Since this specific blueshift would have been easily measured with our data, we do not confirm the value reported by these authors. Nevertheless, our detected 0.16 ± 0.04 Å shift is significant and most likely real, since it is seen even on the transmission spectra without radial-velocity correction. A possible physical explanation is that a net blueshift is imprinted by winds within the exoplanet atmosphere (see Snellen et al. 2010, for a first detection of winds in exoplanets). Theoretical models (e.g., Kempton et al. 2014; Showman et al. 2013) predict a net blueshift due to both planetary rotation and winds in the terminator of the atmosphere (the part we probe with transmission spectroscopy). The blueshift we measured corresponds to a wind speed of 8 ± 2 km s^{-1}. Models typically predict a blueshift of 3 km s^{-1}. However, these winds are estimated for pressures down to $\sim 10^{-5}$–10^{-6} bar. As we show below, our sodium detection allows us to probe pressures of $\sim 10^{-7}$–10^{-9} bar (0.1–0.001 μbar) at an altitude of 10 000 km. We can therefore expect winds stronger than 3 km s^{-1} in the higher atmosphere. This calls for additional theoretical works on winds in the upper atmospheres of exoplanets, and new data to confirm the blueshift value.

3.3. Transmission light-curve analysis

We computed the transmission light-curve of HD 189733b for every observation nights following Sect. 2.6 and for every passbands described in Sect. 3.1. For our analysis, the transit ephemerides were fixed. They are given by the parameters described in Table 2. For the 12 Å passband, we estimated errors on each individual spectrum of 250 ppm to 800 ppm. The propagation of these errors to the time series provides uncertainties of about 100–150 ppm on the values of the baseline and on the absorption depth. This allows us to determine absorption depths of sodium in the exoplanet atmosphere during each night at a level between 1.9 and 5.7σ (see Table 4). Note that when we subtract the best-fit absorption depth, the standard deviation of the residuals is about 550 ppm for each night. When we

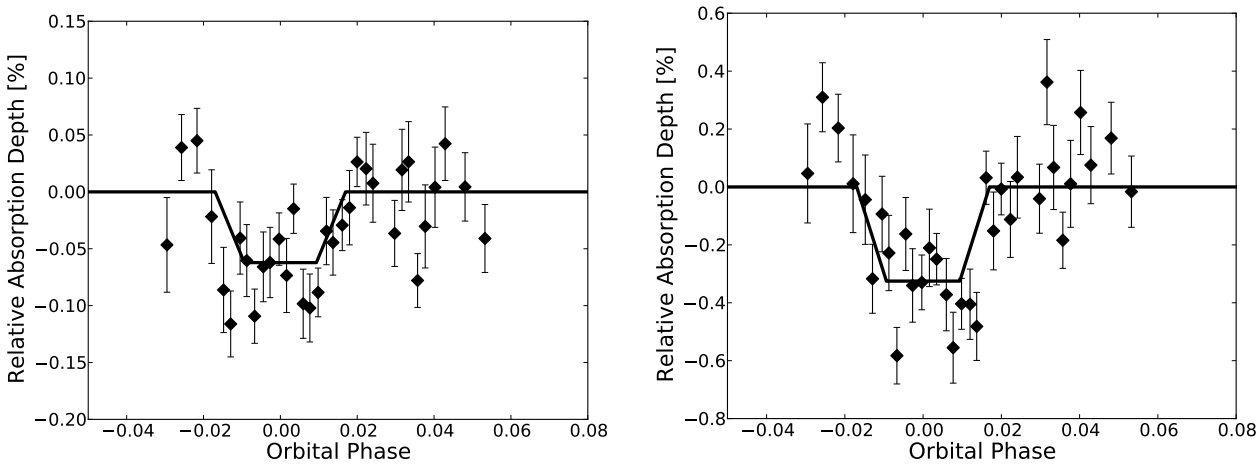

Fig. 3. HARPS transmission light curve of HD 189733b. The three nights are averaged together with bins of 3 spectra. *Left*: relative fluxes are integrated in each spectrum over a 12 Å passband including the whole sodium Na I D doublet and compared to reference passbands in the same spectrum. The overall absorption depth is detected at 620 ppm with 7.8σ. *Right*: relative fluxes are integrated over two passbands of 0.75 Å around each sodium Na I D line. The absorption depth is detected at 3250 ppm with 9.8σ. Note the different vertical scales.

sum the data of the three nights, we obtain an absorption signal of 0.062±0.008% (7.8σ) for the 12 Å passband (Fig. 3). Our best measurement is achieved for the passband of 1.5 = 2 × 0.75 Å and delivers a value of 0.325 ± 0.033% (9.8σ). This perfectly agrees with our transmission spectrum method and shows both the complementarity and the compatibility of the two methods. Compatibility because the measured absorption levels are within a 1σ error bar (see Astudillo-Defru & Rojo 2013), and complementarity because the second method yields line information and demonstrates that the additional absorption is indeed observed during the transit (see also Sect. 3.4). As expected, a small decrease of the measured absorption signal is observed for the smallest passband (0.375 = 2 × 0.188 Å), whose width is commensurable with the wavelength shift imprinted by the radial velocity of the planet. This effect thus results in a flux loss, hence in a weaker signal.

3.4. Systematic effects

Possible systematic errors can be present in the data. To estimate such effects, we performed an empirical Monte Carlo (EMC) analysis for each of our observed transits following Sect. 2.7. This analysis makes us confident that our measured signals is indeed due to the exoplanetary transit and not spurious (e.g., due to other astrophysical effects such as stellar rotation, observational conditions, or instrumental effects). The EMC was performed for both the transmission spectrum and the light-curve methods using 3000 iterations for each scenario described in Sect. 2.7 (in-in, out-out, in-out) and for each night. The standard deviation of the distributions does not increase significantly when the number of iterations is increased.

The results are shown in Fig. 4 and the errors are summarized with all the different methods in Fig. 6. All the in-in and out-out distributions are centered on zero, showing that the measured absorption signal indeed comes from the transit and cannot be explained differently. The in-out distributions are well centered on the value determined by the transmission spectrum and light-curve methods. The errors given by the EMC are larger than the nominal errors (because of the photon noise propagation), but only by a factor of $\lesssim$2. This shows that while systematic errors are present in our data, they do not undermine our detection. The empirical Monte Carlo simulation described above supports the hypothesis that the detected signal originates from a transit.

We also computed false-alarm probabilities for each night for both the transmission spectrum and the light-curve methods. We performed 10 000 iterations and found false-alarm probabilities to our sodium detection of ∼0.5%, ∼9%, and $\lesssim$0.01% for night 1, 2, and 3 respectively (see Fig. 5). Adding all the nights yields a false-alarm probability of $\lesssim$0.01%.

4. Discussion

4.1. Summary of the Na I D detection

A summary of our results is shown in Fig. 6. All the different methods for measuring the transit depth $\delta(\Delta\lambda)$ in a given wavelength bin $\Delta\lambda$ are shown individually for each night and also for the combined data set for the 1.5 = 2 × 0.75 Å and 12 Å passbands.

We highlight several aspects: First, correcting the telluric lines is mandatory. In fact, water lines around the sodium Na I D doublet imprint spurious systematics in any possible direction. This depends on whether the transit is observed at lower or higher airmass than the out-of-transit data and on the value of the barycentric Earth radial velocity (BERV). The BERV causes the telluric lines to fall at different places on the stellar spectra. For a fixed choice of passbands, a given telluric line may not be always included. This means that the ratio of the reference passbands, which contain other telluric lines, can be affected in any direction. For example, during night 3, the signal measured without telluric correction is, by chance, the same signal as measured after telluric correction because the positions of the telluric lines in the transmission spectrum do not affect the extraction of the sodium signal. The correction for night 2 is less reliable than that of the two other nights because we lack a baseline before the transit. This implies that we probably over-corrected the data taken during this night, hence the measured value is underestimated. Second, the absorption depths measured with transmission-spectra and light-curve methods are consistent with each other within the same night. Third, systematic effects are different from night to night. Nights 2 and 3 were probably more stable than night 1. Systematics in night 1 are probably also stronger as a result of the low cadence of the observations.

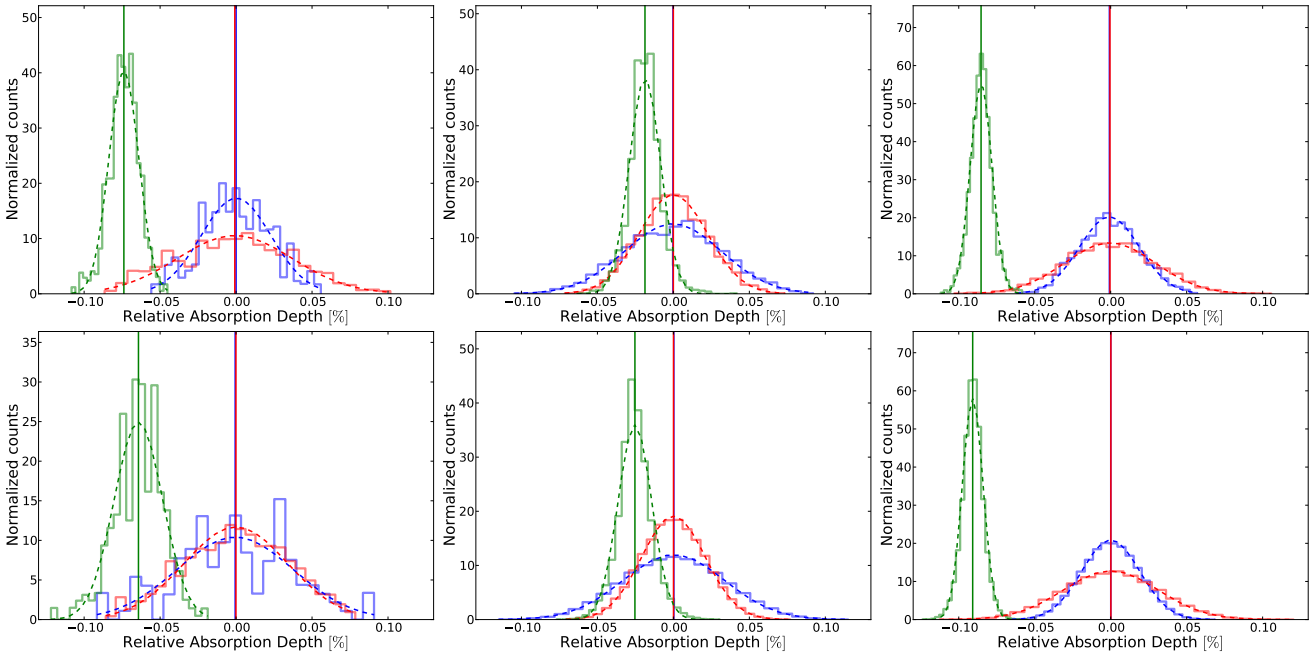

Fig. 4. Distributions of the empirical Monte Carlo analysis for the 12 Å passband. *Top row*: results for the transmission spectrum method. *Bottom row*: results for the light-curve method. The columns correspond to the three different observation nights (nights 1 to 3, *from left to right*). In-in, out-out and in-out scenarios are shown in blue, red, and green. Distributions are shown as continuous lines, the Gaussian fit to the distribution as dotted lines, and vertical lines are the average values. Results on the measurements and errors caused by these distributions are summarized in Fig. 6, where we compare it to the nominal values.

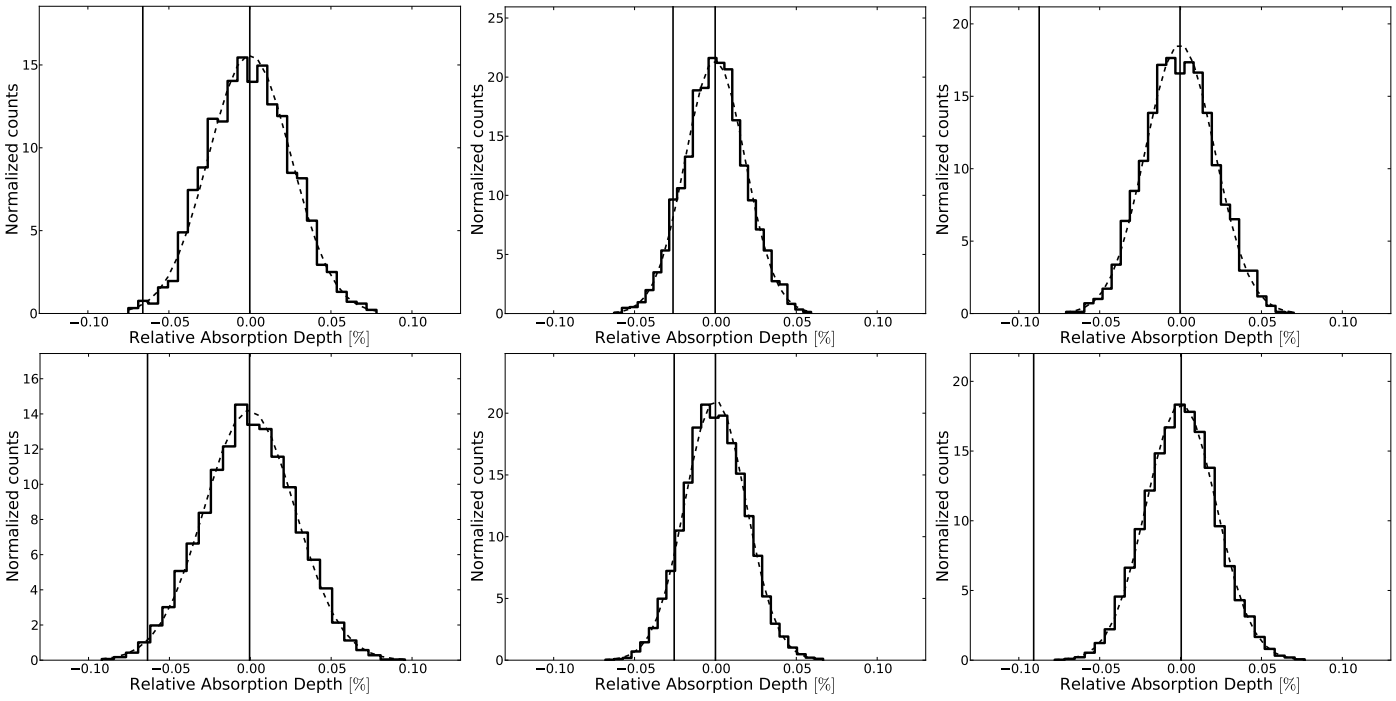

Fig. 5. Distributions of the false-alarm probability analysis for the 12 Å passband. *Top row*: results for the transmission spectrum method. *Bottom row*: results for the light-curve method. The columns correspond to the three different observation nights (night 1 to 3, *from left to right*). Distributions are shown as continuous lines, the Gaussian fit as dotted lines, and the nominal values from which the false-alarm probabilities are inferred as vertical lines.

Even if similar S/Ns are reached in the three different nights, it seems that it is better to have a high-cadence observational strategy (provided all the spectra have a S/N above a certain threshold). We also note that the measured values are different for different nights. At this level of precision, and assuming we efficiently correct for systematics, we cannot exclude intrinsic variability related to the stellar or planetary properties. Our results favor a variation from night to night within 1–2σ. We did not take into account the potential effect of a differential limb-darkening or of the Rossiter-McLaughlin effect. However, the

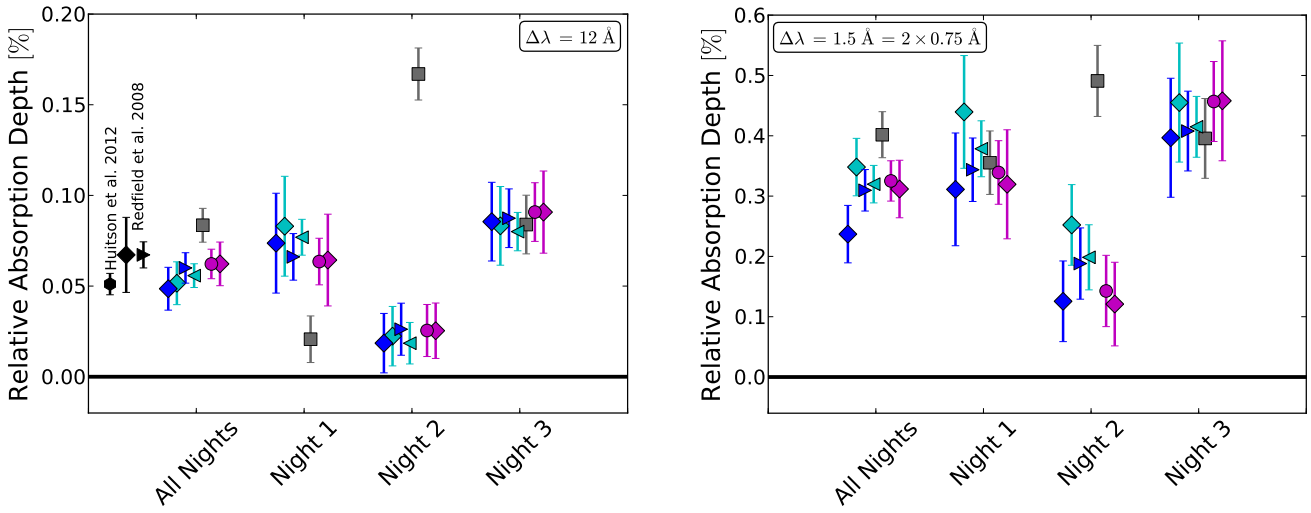

Fig. 6. Comparison of the different methods. The relative absorption depth of the sodium lines are shown for all the nights and for the different methods. Gray squares are the measurement levels without any correction. Particularly, telluric lines imprint spurious systematics in any directions. Magenta circles and diamonds are measurements made with the light-curve method and the empirical Monte Carlo analysis. The blue left triangle and diamond are for the transmission spectrum without radial-velocity correction and the corresponding empirical Monte Carlo analyses. The cyan right triangles and diamonds are for the transmission spectrum with planetary radial-velocity correction and the corresponding empirical Monte Carlo analysis. The total absorption depth when adding the entire night are also indicated. *Left*: summary for the 12 Å passband. The measurement of Huitson et al. (2012; 3 transits with HST/STIS) is shown as a black hexagon. The measurement of Redfield et al. (2008; 35 exposures in-transit (600 s) observed during 11 transit events) is shown as the black left triangle and diamond. The errors correspond to their photon noise and empirical Monte Carlo analysis. The HARPS precision is comparable with the HST/STIS precision, which shows the importance of ground-based high-resolution observations of exoplanetary atmospheres. *Right*: summary of the 1.5 = 2 × 0.75 Å passband.

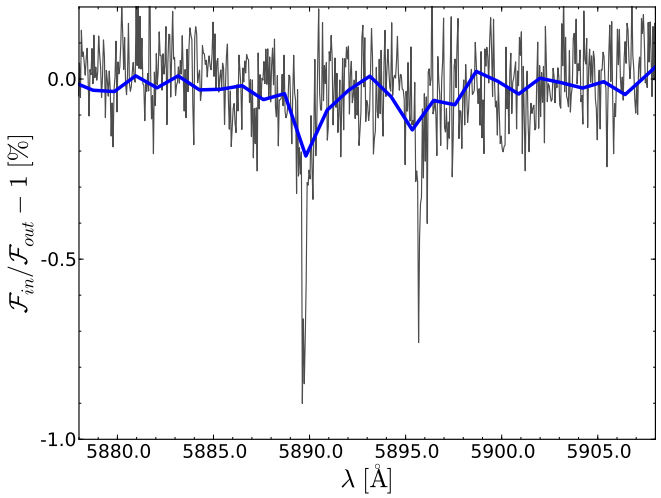

Fig. 7. Comparison of the transmission spectra around the Na I doublet obtained by the HST/STIS instrument (Huitson et al. 2012, in blue) and by the HARPS spectrograph (binned by 5×, in black).

impact of differential limb-darkening should be an order of magnitude lower than the achieved precision (Charbonneau et al. 2002; Redfield et al. 2008). On the other hand, the Rossiter-McLaughlin effect can mimic an exoplanetary atmospheric absorption and imprint features at similar level in a transmission spectrum. This should average out during a whole transit, however, if the exposures are equally distributed over the transit (Dravins et al. 2014). This is the case for our three analyzed transit events. Finally, we would like to point out that the precision obtained from summing all the nights is comparable with the HST/STIS precision (with the same number of observed transits) or with 10 m size telescopes. This highlights the potential of ground-based high-resolution observations of exoplanetary atmospheres from 4 m telescopes.

As mentioned before, we obtain the same precision in our detection (0.056 ± 0.007%) as in the HST/STIS measurements of Huitson et al. (2012; 0.051 ± 0.006%) on a relatively wide passband (here the "12 Å"). We can take advantage of the high spectral resolution of HARPS ($\mathcal{R}$ ∼ 115 000), compared to HST/STIS ($\mathcal{R}$ ∼ 5500) to characterize the narrow line cores of the Na I doublet and, as a consequence, explore higher regions in the atmosphere of HD 189733b.

The haze in the HD 189733b atmosphere has previously been deduced from low-resolution spectra covering much broader spectral regions than the one considered here (e.g., in Lecavelier Des Etangs et al. 2008a; Pont et al. 2013). Rayleigh scattering by hazes dominates the transmission spectrum in the optical, only allowing the narrow core of the sodium lines to be observed at high spectral resolution. This is indeed what we observe in our data.

As described in Sect. 3.1, we computed different absorption depths $\delta(\Delta\lambda)$ for different passbands (summary in Tables 3 and 4). The absorption depth increases for narrow passbands. This shows that most of the signal we measure originates in the narrow line cores (≤1 Å), even if a small portion of the absorption comes from a broader component. A Gaussian fitted to each line yields a full width at half maximum (FWHM) of 0.52 ± 0.08 Å (see Fig. 2). A comparison to the resolution element of 0.05 Å (2.7 km s^{-1}) shows that the lines are resolved by a factor of ∼10 (see Fig. 7). The same fit allows us to measure absorption depths in the core of the two Na I D lines of 0.64 ± 0.07% and 0.40 ± 0.07% for the D2 and D1 lines, respectively.

4.2. Na I D doublet as a probe of the upper atmosphere

We compared our measurements with transmission spectroscopy models. We used the η model described in Ehrenreich et al. (2006, 2012, 2014). The model computes the opacity along the

Table 5. Choice of the wavelength ranges for the atmospheric model fits, number of Na I lines FWHM encompassed in the wavelength ranges, corresponding altitudes, and fitted temperatures.

Model atmospheres	Wavelength ranges [Å]	# Na I D's *FWHM*	Corresponding altitude [km]	Fitted temperature [K]
Model 0	5870.00–5882.22 5903.24–5916.00	–	0	1140
Model 1 (Wing'shoulders)	5882.22–5889.22 5890.26–5895.20 5896.24–5903.24	2–14	1500 ± 1500	1630 ± 70
Model 2a (D1 core)	5895.20–5895.46 5895.98–5896.24	1–2	2700 ± 800	1700 ± 320
Model 2b (D2 core)	5889.22–5889.48 5890.00–5900.26	1–2	3800 ± 900	2170 ± 320
Model 3a (D1 core)	5895.46–5895.67 5895.77–5895.98	0.2–1	5100 ± 3100	2220 ± 340
Model 3b (D2 core)	5889.48–5889.69 5889.79–5890.00	0.2–1	7900 ± 5500	3220 ± 270
Model 4a (D1 core)	5895.67–5895.77	⩽0.2	9800 ± 2800	2600 ± 600
Model 4b (D2 core)	5889.69–5889.79	⩽0.2	12 700 ± 2600	3270 ± 330

Notes. We centered the wavelength ranges on the center of each sodium line in the planet rest frame taking into account the observed blueshift.

line of sight grazing the atmospheric limb of the planet and integrates over the whole limb. The planetary atmosphere is modeled as a perfect gas in hydrostatic equilibrium composed of 93% of molecular hydrogen and, 7% of helium, and a solar abundance of atomic sodium (volume-mixing ratio of 10^{-6}). Several model atmospheres are simulated with isothermal temperature profiles for temperatures ranging from 1000 K to 3600 K by step of 100 K. To increase the resolution in temperature, we interpolated linearly between the models. The sodium line profiles were modeled with Voigt functions resulting from the convolution of a Doppler thermal profile (dominating the line cores) and a Lorentzian profile accounting for the natural and collisional broadenings in the line wings. Collisional or pressure broadening completely dominates the line shapes far (over scales of ∼100 nm) from the cores (Iro et al. 2005). The half-width at half-maximum (HWHM) of the pressure-broadened Lorentzian follows the prescriptions of Burrows et al. (2000) and Iro et al. (2005), which are valid over the wavelength range we studied. The modeled transmission spectra, calculated at a resolution of 0.01 Å, were convolved with the average HARPS line spread function (LSF), which is well represented by a Gaussian with a width of 0.05 Å. In contrast to HST/STIS, the comparison between the models and our data is facilitated by HARPS resolving individual lines that arise in the planet atmosphere by a factor ∼10 (see above).

Before comparing our transmission spectrum to models, we first fit a simple haze model to our data. We know that the Rayleigh slope in our wavelength range analysis is negligible, therefore hazes can be well represented by an absorption cut-off at a given level. This level must be compatible with our measured continuum, which corresponds to the wavelength ranges of model 0 in Table 5. We also wish to determine whether the sodium wing absorption dominates the haze absorption in the transmission spectrum. The wing-shoulder region is described by the wavelength ranges of model 1 in Table 5. Therefore, the highest altitude of the cloud deck that is compatible with the continuum level is given by a constant fit to the wavelength regions used to fit model atmospheres 0 and 1 to the data. This constant level gives a Bayesian information criterion (BIC) of 1 597 in the wing region (region 1).

To compare our observed transmission spectrum to models, our approach was to fit the different regions of the measured transmission spectrum around the sodium doublet with model atmospheres with different isothermal profiles. We divided the transmission spectrum into separate wavelength ranges around each line of the sodium doublet, each corresponding to altitude slices. The altitude slices are given by the maximum between the altitude errors on the data and the difference in altitudes in the given ranges. These ranges are listed in Table 5. We fit these different parts of the spectrum with different isothermal models, probing separately the line cores (models 4), the region encompassed within $1 \times FWHM$ (excluding the line cores; models 3), the region between 1× and 2× the FWHM (models 2), the line wings (excluding the previous regions; model 1), and the continuum (model 0). All the fits were obtained with a χ^2 minimization over the grids of atmospheric models obtained by varying the temperature and a general offset in relative flux. In the continuum wavelength range we cannot see a significant sodium absorption due to absorbing wings. Therefore we chose model 0 with a fixed temperature of 1140 K (the equilibrium temperature of HD 189733b). The fit of this model to the continuum allowed us to determine the offset in planetary radius between the data and the models. We fixed this offset for the subsequent model adjustments. We fit models 1, 2, 3, and 4 to their respective spectral regions by considering the model temperature as a free parameter. The fit of model 1 yields a temperature of 1630 K for a BIC of 1542. The comparison with the BIC of 1597 obtained with a constant haze level is very strong evidence ($\Delta BIC \geq 20$) in favor of a scenario where the Na I wing absorption dominates the haze absorption. Thus, part of our measured sodium absorption is due to the wings and corresponds to lower altitudes and temperatures. The three other models (2, 3, and 4) investigate different parts of the line cores inside 1 Å (2 *FWHM*, see Table 5). The best-fit models are shown in Fig. 8. For each range of altitudes, we therefore derived one temperature. The resulting temperature profile as a function of altitude is shown in Fig. 9. The temperature linearly increases with altitude with a gradient of ∼0.2 K km^{-1} (0.2 ± 0.1 K km^{-1}). Note that our measured temperatures are underestimated because we used isothermal models, which yield for the same upper temperature more extended atmospheres than models with positive temperature gradient.

Our high-resolution measurement of sodium in HD 189733b allowed us to probe a new atmospheric region (between ∼1.1–1.2 planetary radius, corresponding to pressures

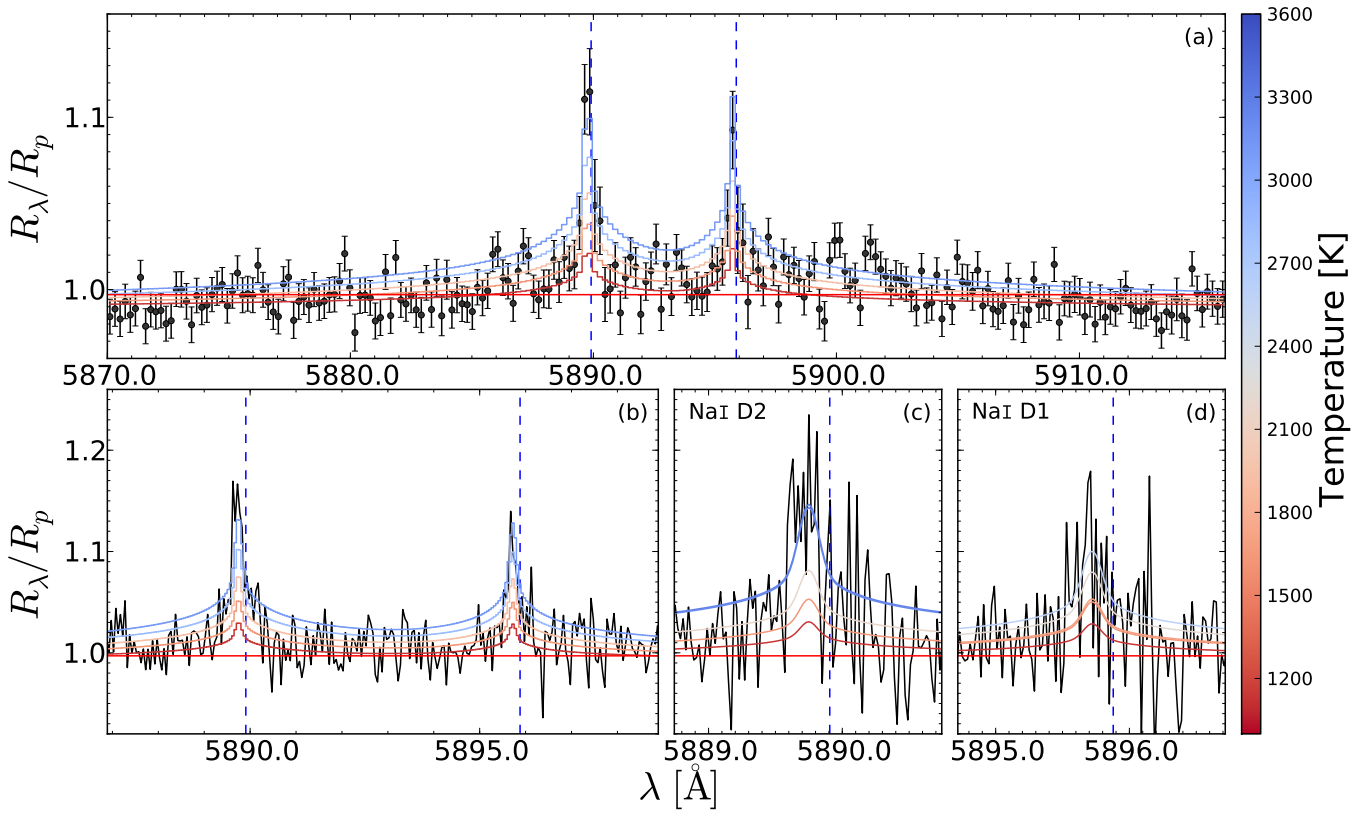

Fig. 8. Fit of a range of η models to the HARPS transmission spectra of HD 189733b. The data and models are binned by 20× (panel **a)**), 5× (panel **b)**) and 2× (panels **c)** and **d)**). Models correspond to those described in Table 5. Some additional models (2100 K, 2600 K, 3100 K, the hottest in panels **a)** and **b)** and the continuum level (in red), which correspond to the altitudes of a haze layer deck, are also shown for comparison. Our analysis shows that the atmosphere of HD 189733b is not isothermal.

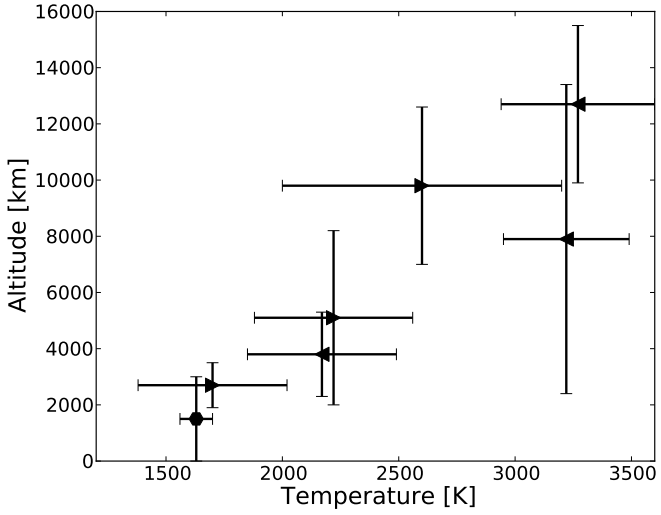

Fig. 9. Temperature profile obtained by our fitting process of η models to the transmission spectrum. The right and left triangle correspond to the Na I D1 and D2 lines. The diamond correspond to the wing shoulders. A temperature gradient of ~0.2 K km^{-1} is measured.

of 10^{-7}–10^{-9} bar) above the result previously obtained at lower resolution (Huitson et al. 2012). Our results suggest that a part of the sodium absorption occurs in the (lower) thermosphere, where heating by the stellar X/EUV photons occurs (Lammer et al. 2003; Yelle 2004; Vidal-Madjar et al. 2011; Koskinen et al. 2013). Our interpretation relies on hydrostatic models, however, which might be questionable at very high altitudes. A more detailed theoretical analysis of these results is developed in a separate paper (Heng et al. 2015).

5. Conclusions

We have presented an analysis of all the available transit observations of HD 189733b with HARPS at the ESO 3.6 m telescope. We carefully corrected for the change in radial velocity of the planet and for telluric contamination, fully exploiting the high spectral resolution and the stability of HARPS. We detected absorption excess of the Na I D lines in our transmission spectrum. We measured line contrasts of 0.64 ± 0.07% (D2) and 0.40 ± 0.07% (D1) and FWHMs of 0.52 ± 0.08 Å. Sodium is clearly detected over several different passbands, and the signatures are robust against different statistical tests. Moreover, these detections are consistent and comparable in terms of precision with those obtained from space-borne or 10 m class ground-based facilities.

The high resolution permits us to measure a blueshift in the line positions of 0.16 ± 0.04 Å. We interpreted this as wind in the upper layer of the atmosphere of a velocity of 8 ± 2 km s^{-1}. Because we resolved the sodium lines, we used them as a probe of the lower pressure part of the atmosphere. We measured a nonisothermal temperature profile inside our range of probed altitudes, where the sodium absorption peaks above the haze in the atmosphere. We found that the temperature increases toward the thermosphere. A temperature gradient of ~0.2 K km^{-1} was measured. This positive temperature gradient does not depend on assumptions about the haze layer. The gradient can be measured from the resolved line cores and in particular from the difference in absorption levels between the D1 and the D2 lines. This

shows that beyond detecting atomic species, transit spectroscopy allows characterizing physical conditions in atmospheres.

These transit spectroscopy data were previously used by Triaud et al. (2009) and by Collier Cameron et al. (2010) to study the Rossiter-McLaughlin effect. Furthermore, with these same observations Di Gloria (in prep.) detected a slope in the ratios of the planet-star radius that Pont et al. (2008, 2013) interpreted as Rayleigh scattering. These studies demonstrate the relevance of studying exoplanet atmospheres with high-resolution spectrographs mounted on 4-m-class telescopes. This is especially important considering that several such facilities will be built in the coming years to prepare for the follow-up of exoplanet candidates from incoming space missions such as K2 (on-going), TESS, CHEOPS, and PLATO.

In the near future, the HARPS-like instrument ESPRESSO will be mounted on the Very-Large Telescope (VLT) incoherent focus. ESPRESSO will be able to probe exoplanetary atmospheres in the optical. This will bring a more complete census of the chemical composition and study of aeronomic properties of a large variety of exoplanets, including those with higher bulk densities or with fainter host stars. Several spectrographs will be built soon to conduct investigations in the infrared, such as SPIROU, CARMENES, IRD and CRIRES+. Judging from recent results (e.g., Birkby et al. 2013; Snellen et al. 2014), a strong development of atmospheric detections and characterization in the infrared is possible. Eventually, high-resolution spectra of exoplanets with broad spectral coverage will allow collating an inventory of the atmospheric chemical composition, will help explore aeronomic properties such as pressure-temperature profiles, and will lead to a better understanding of the formation and evolution of exoplanets. This is also a motivation for building a high-resolution spectrograph on the European Extremely-Large-Telescope such as HiReS and METIS (Udry et al. 2014; Brandl et al. 2014; Snellen et al. 2015). In the meantime, extensive studies have to be made with existing facilities and data especially in the optical domain (e.g., Hoeijmakers et al. 2015) to help observers make the best use of future facilities. Our study is a significant step in this direction. It could be extended to searching for other species or as a systematic search in other hot-Jupiter atmospheres.

Acknowledgements. This work has been carried out within the frame of the National Centre for Competence in Research "PlanetS" supported by the Swiss National Science Foundation (SNSF). The authors acknowledge the financial support of the SNSF. We thank M. Mayor, A. H. M. J. Triaud, and A. Lecavelier for obtaining the data. We thank K. Heng, S. Khalafinejad, E. Di Gloria, V. Bourrier, and R. Allart for discussions and insights. We gratefully acknowledge our referee, I. A. G. Snellen, for valuable comments that improved our manuscript.

References

Agol, E., Cowan, N. B., Knutson, H. A., et al. 2010, ApJ, 721, 1861
Astudillo-Defru, N., & Rojo, P. 2013, A&A, 557, A56
Birkby, J. L., de Kok, R. J., Brogi, M., et al. 2013, MNRAS, 436, L35
Boisse, I., Moutou, C., Vidal-Madjar, A., et al. 2009, A&A, 495, 959
Bouchy, F., Udry, S., Mayor, M., et al. 2005, A&A, 444, L15
Brandl, B. R., Feldt, M., Glasse, A., et al. 2014, in SPIE Conf. Ser., 9147, 21
Brogi, M., Snellen, I. A. G., de Kok, R. J., et al. 2012, Nature, 486, 502
Brown, T. M. 2001, ApJ, 553, 1006
Burrows, A., Marley, M. S., & Sharp, C. M. 2000, ApJ, 531, 438
Burton, J. R., Watson, C. A., Rodríguez-Gil, P., et al. 2015, MNRAS, 446, 1071
Charbonneau, D., Noyes, R. W., Korzennik, S. G., et al. 1999, ApJ, 522, L145
Charbonneau, D., Brown, T. M., Noyes, R. W., & Gilliland, R. L. 2002, ApJ, 568, 377
Collier Cameron, A., Bruce, V. A., Miller, G. R. M., Triaud, A. H. M. J., & Queloz, D. 2010, MNRAS, 403, 151
Deming, D., Wilkins, A., McCullough, P., et al. 2013, ApJ, 774, 95
Dravins, D., Ludwig, H.-G., Dahlén, E., & Pazira, H. 2014, Proc. Lowell Observatory, eds. G. van Belle, & H. Harris [arXiv:1408.1402]
Ehrenreich, D., Tinetti, G., Lecavelier Des Etangs, A., Vidal-Madjar, A., & Selsis, F. 2006, A&A, 448, 379
Ehrenreich, D., Vidal-Madjar, A., Widemann, T., et al. 2012, A&A, 537, L2
Ehrenreich, D., Bonfils, X., Lovis, C., et al. 2014, A&A, 570, A89
Heng, K., & Showman, A. P. 2014, Ann. Rev. Earth Planet. Sci., 43
Heng, K., Wyttenbach, A., Lavie, B., et al. 2015, ApJ, accepted [arXiv:1503.05582]
Hinkle, K. H., Wallace, L., & Livingston, W. 2003, in BAAS, 35, 1260
Hoeijmakers, H. J., de Kok, R. J., Snellen, I. A. G., et al. 2015, A&A, 575, A20
Huitson, C. M., Sing, D. K., Vidal-Madjar, A., et al. 2012, MNRAS, 422, 2477
Iro, N., Bézard, B., & Guillot, T. 2005, A&A, 436, 719
Jensen, A. G., Redfield, S., Endl, M., et al. 2011, ApJ, 743, 203
Kempton, E. M.-R., Perna, R., & Heng, K. 2014, ApJ, 795, 24
Khalafinejad, S. 2013, Master's Thesis, Universiteit Leiden
Koskinen, T. T., Harris, M. J., Yelle, R. V., & Lavvas, P. 2013, Icarus, 226, 1678
Kreidberg, L., Bean, J. L., Désert, J.-M., et al. 2014, Nature, 505, 69
Lammer, H., Selsis, F., Ribas, I., et al. 2003, ApJ, 598, L121
Langland-Shula, L. E., Vogt, S. S., Charbonneau, D., Butler, P., & Marcy, G. 2009, ApJ, 696, 1355
Lecavelier Des Etangs, A., Pont, F., Vidal-Madjar, A., & Sing, D. 2008a, A&A, 481, L83
Lecavelier Des Etangs, A., Vidal-Madjar, A., Désert, J.-M., & Sing, D. 2008b, A&A, 485, 865
Madhusudhan, N., Knutson, H., Fortney, J., & Barman, T. 2014, Protostars and Planets VI, eds. H. Beuther, R. S. Klessen, C. P. Dullemond, & T. Barman (Tucson: University of Arizona Press), 914, 739
Marley, M. S., Gelino, C., Stephens, D., Lunine, J. I., & Freedman, R. 1999, ApJ, 513, 879
Mayor, M., Pepe, F., Queloz, D., et al. 2003, The Messenger, 114, 20
Moutou, C., Coustenis, A., Schneider, J., et al. 2001, A&A, 371, 260
Murgas, F., Pallé, E., Zapatero Osorio, M. R., et al. 2014, A&A, 563, A41
Narita, N., Suto, Y., Winn, J. N., et al. 2005, PASJ, 57, 471
Nikolov, N., Sing, D. K., Pont, F., et al. 2014, MNRAS, 437, 46
Pepe, F., Ehrenreich, D., & Meyer, M. R. 2014, Nature, 513, 358
Pont, F., Knutson, H., Gilliland, R. L., Moutou, C., & Charbonneau, D. 2008, MNRAS, 385, 109
Pont, F., Sing, D. K., Gibson, N. P., et al. 2013, MNRAS, 432, 2917
Redfield, S., Endl, M., Cochran, W. D., & Koesterke, L. 2008, ApJ, 673, L87
Seager, S., & Sasselov, D. D. 2000, ApJ, 537, 916
Showman, A. P., Fortney, J. J., Lewis, N. K., & Shabram, M. 2013, ApJ, 762, 24
Sing, D. K., Vidal-Madjar, A., Désert, J.-M., Lecavelier des Etangs, A., & Ballester, G. 2008a, ApJ, 686, 658
Sing, D. K., Vidal-Madjar, A., Lecavelier des Etangs, A., et al. 2008b, ApJ, 686, 667
Sing, D. K., Huitson, C. M., Lopez-Morales, M., et al. 2012, MNRAS, 426, 1663
Sing, D. K., Wakeford, H. R., Showman, A. P., et al. 2015, MNRAS, 446, 2428
Snellen, I., de Kok, R., Birkby, J., et al. 2015, A&A, 576, A59
Snellen, I. A. G., Albrecht, S., de Mooij, E. J. W., & Le Poole, R. S. 2008, A&A, 487, 357
Snellen, I. A. G., de Kok, R. J., de Mooij, E. J. W., & Albrecht, S. 2010, Nature, 465, 1049
Snellen, I. A. G., Brandl, B. R., de Kok, R. J., et al. 2014, Nature, 509, 63
Torres, G., Winn, J. N., & Holman, M. J. 2008, ApJ, 677, 1324
Triaud, A. H. M. J., Queloz, D., Bouchy, F., et al. 2009, A&A, 506, 377
Udry, S., Lovis, C., Bouchy, F., et al. 2014 [arXiv:1412.1048]
Vidal-Madjar, A., Lecavelier des Etangs, A., Désert, J.-M., et al. 2003, Nature, 422, 143
Vidal-Madjar, A., Arnold, L., Ehrenreich, D., et al. 2010, A&A, 523, A57
Vidal-Madjar, A., Sing, D. K., Lecavelier Des Etangs, A., et al. 2011, A&A, 527, A110
Wood, P. L., Maxted, P. F. L., Smalley, B., & Iro, N. 2011, MNRAS, 412, 2376
Yelle, R. V. 2004, Icarus, 170, 167
Zhou, G., & Bayliss, D. D. R. 2012, MNRAS, 426, 2483